Straylight analyses and mitigation strategies for the ELT METIS instrument

Eduard Muslimov, Tibor Agócs, Ivan Lloro, Adrian Glauser, Olivier Absil, et al.

SPIE. Event: SPIE Optical Systems Design, 2021, Online Only

Straylight analyses and mitigation strategies for the ELT METIS instrument

Eduard Muslimov[a,b,c], Tibor Agócs[a], Ivan Lloro[a], Adrian M. Glauser[d], Olivier Absil[e], Dennis Dolkens[a], Niels Tromp[a], and Daan Zaalberg[a]

[a]NOVA Optical IR Instrumentation Group at ASTRON Oude Hoogeveensedijk 4, 7991 PD Dwingeloo, The Netherlands
[b]Aix Marseille Univ, CNRS, CNES, LAM, Marseille, France
[c]Kazan National Research Technical University named after A.N. Tupolev KAI, 10 K. Marx, Kazan, Russia, 420111
[d]Institute for Particle Physics and Astrophysics, ETH Zurich, Wolfgang-Paulistr. 27, 8093 Zurich, Switzerland
[e]Space sciences, Technologies, and Astrophysics Research (STAR) Institute, Universite deLiege, 19c allee du Six Aout, B-4000 Sart Tilman, Belgium

ABSTRACT

The Mid-infrared ELT Imager and Spectrograph (METIS) is one of the three first-generation instruments on the Extremely Large Telescope (ELT). It will provide 20 instrument configurations for direct and high-contrast imaging, medium and high resolution spectroscopy in the wavelength range of $3 - 13\mu m$. The straylight will affect the image contrast and objects recognition thus influencing the final instrument performance. For this reason it should be taken into account and accurately modeled at the design stage. In the present study we consider straylight from the following sources: surface roughness and defects of the optical surfaces, multiple reflections and diffraction, which will all influence the instrument performance. We estimate their influence using a bottom-up modelling approach at the system level and derive the requirements for some critical parameters. Using empirical and analytical models and performing non-sequential raytracing we demonstrate that the target straylight level can be reached in the current design with reasonable specifications on the optical components.

Keywords: ELT, Mid-infrared ELT Imager and Spectrograph (METIS), straylight, scattering, high contrast imaging

1. INTRODUCTION

The Mid-infrared ELT Imager and Spectrograph (METIS) of the European Southern Observatorie's (ESO) Extremely Large Telescope (ELT) consists of diffraction-limited imagers that cover 3 to 13 microns with medium resolution (R~5000) longslit spectroscopy and an integral field spectrograph for high spectral resolution spectroscopy (R~100,000) over the L and M bands.[1] The final instrument performance is influenced by straylight coming from different origins, which must be taken into account already at the design stage. In the present paper we analyze the straylight using bottom-up approach at the system level in order to estimate the expected performance and derive some critical requirements to the subsystems, elements and additionally AIV related information e.g. related to handling at different manufacturing and integration stages.

METIS has 20 instrument configurations and includes 5 optical subsystems. The entire instrument block diagram with the cardinal optical points and planes as intermediate stops and focii is shown in Figure 1. The parts directly considered in the analysis below are highlighted by dashed lines. More details on the instrument system design can be found in other sources.[1,2]

Further author information: (Send correspondence to E. Muslimov)
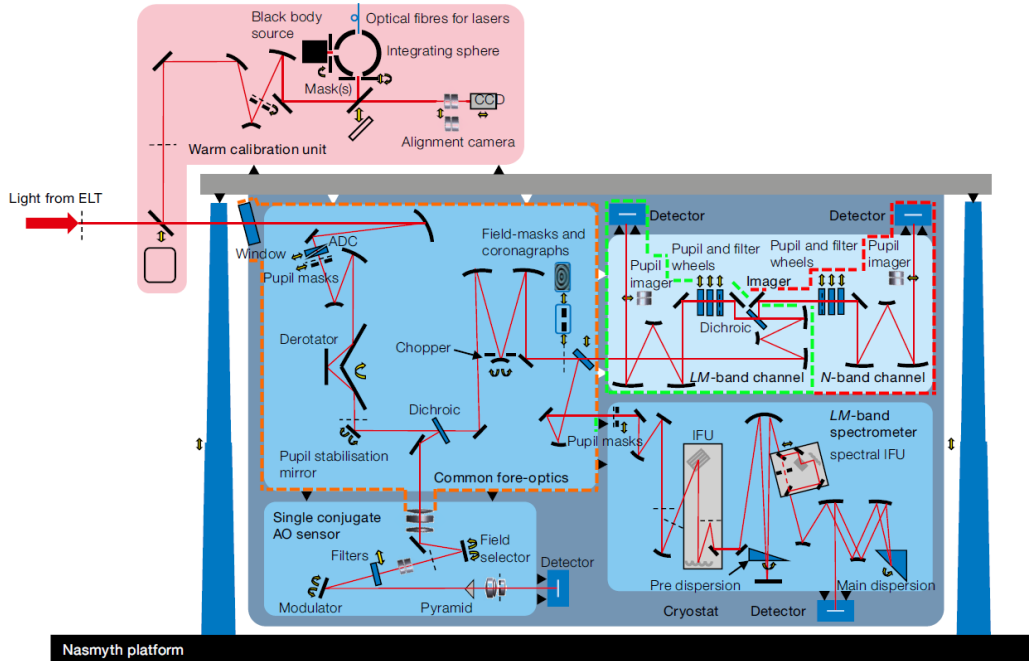E.M.: E-mail: muslimov@astron.nl

Figure 1. The METIS optical system block diagram.

The straylight analysis in such a complex instrument becomes a non-trivial task. We limit the number of straylight sources to those, which were explicitly identified by the science groups and defined in the instrument technical specification. This implies that the analysis is focused on the straylight coming from stellar sources. The direct imaging and high contrast imaging (HCI) modes are considered separately. The spectroscopic modes are not considered since it is assumed that the spectrographs use spatial filters i.e. entrance slits, which allows to perform the analysis independently on subsystem level. For this reason the grisms and high resolution grating are not considered in our analyses (IMG-3 is excluded). Finally, preliminary estimations shown that the influence of contamination and surface imperfections on the direct imaging performance is negligible, while in the HCI modes it is important (IMG-4 is excluded). With all of the mentioned presumptions, the straylight analysis modes are reduced to those shown in Figure 2. This classification is also convenient since every mode requires a separate system model configuration and the simulation technique. According to the instrument specification we set uo the following target straylight levels for different modes:

- The relative scattering intensity in the direct imaging mode should be below 10^{-3} (IMG-1).

- The residual ghosts in the imaging mode should be be less than 5% of the background structure or below the detectors sensitivity level (IMG-2).

- Irradiance from sources outside the input beam envelope should be attenuated by factor of 10^4 (IMG-5).

- All the straylight features in the HCI modes within the dark hole, which is 0.85 (arcsec) at 4 (µm), 2.6 (arcsec) at 12 (µm), should be fainter thab 1^{-5} (HCI-1 to 5).

In general, METIS includes such subsystems as common fore-optics (CFO), imager (IMG) with two branches working in the LM and N wavebands, LM-band spectrograph (LMS), single-conjugate adaptive optics (SCAO) and warm calibration unit (WCU). As it is stated above, LMS is not considered for the system level stray light analyses, except for the pick-off mirror at CFO focal plane (FP2) sending radiation to the LMS. Similarly, we don't consider the SCAO system, since it operates in a different waveband. The only remaining element is the dichroic beam-splitter used to feed SCAO. Finally, WCU is not included in the models, since all the requirements

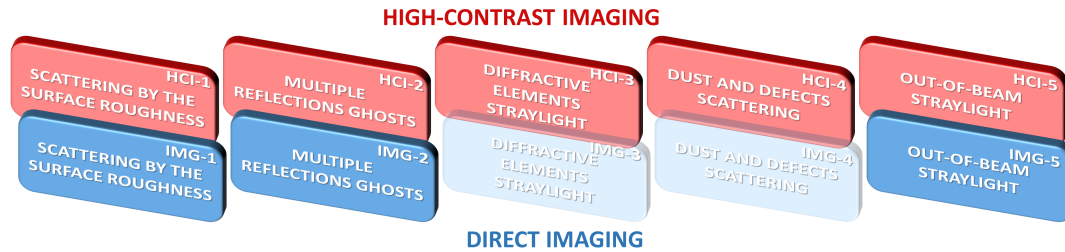| HCI-1 SCATTERING BY THE SURFACE ROUGHNESS | HCI-2 MULTIPLE REFLECTIONS GHOSTS | HCI-3 DIFFRACTIVE ELEMENTS STRAYLIGHT | HCI-4 DUST AND DEFECTS SCATTERING | HCI-5 OUT-OF-BEAM STRAYLIGHT |
| IMG-1 SCATTERING BY THE SURFACE ROUGHNESS | IMG-2 MULTIPLE REFLECTIONS GHOSTS | IMG-3 DIFFRACTIVE ELEMENTS STRAYLIGHT | IMG-4 DUST AND DEFECTS SCATTERING | IMG-5 OUT-OF-BEAM STRAYLIGHT |

DIRECT IMAGING

Figure 2. The METIS straylight analysis modes classified by the source and modelling algorithm.

are defined for on-sky operation. So the model is reduced to the configuration shown in Figure 3. The subsytem colorcode is identical to that in Figure 1.

This figure also demonstrates the simplifications of the mechanical structure representation around the CFO and IMG subsystems. It is modelled as a solid body, having the outer dimensions of the instrument cryostat and a tunnel following the beam inside. The tunnel's geometry follows the full mechanical apertures of the components. In addition, annular diaphragms are introduced to cover the side surfaces of the transmission components. All of these mechanical parts are perfectly absorbing. This simplified model is common for the most of the analyses described below.
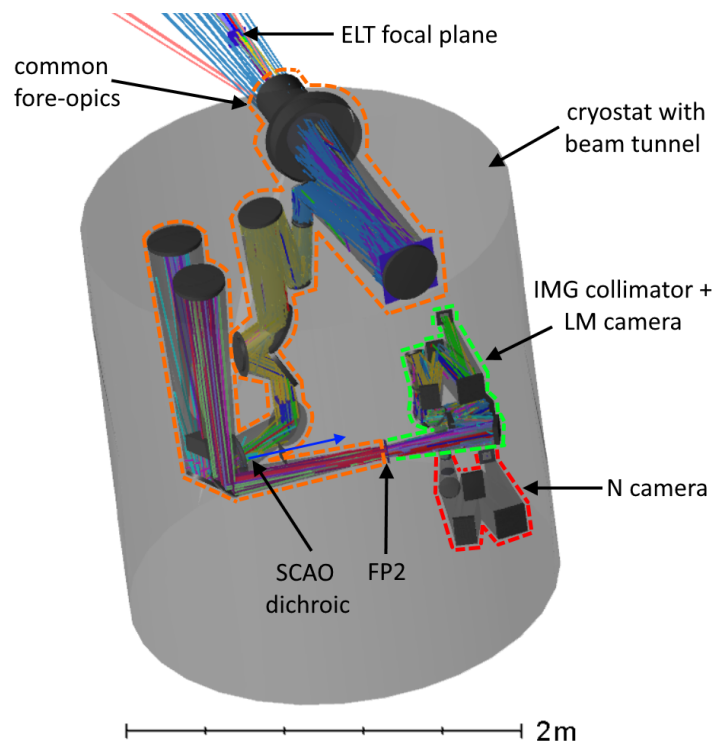

Figure 3. METIS subsystems arrangement and the simplified mechanical model.

Another common presumption relates to the radiation sources. In all the analyses the simulation is performed for monochromatic sources at two wavelengths to probe the LM and N bands. The source flux power in each case corresponds to reaching the detector saturation. Thus for the LM band L' filter represented by the central wavelength as a monochromatic source at 3.87 (µm) with $7.956 \cdot 10^{-12}$ (W) power is used. Similarly, in the N band we use N_2 filter centred around 11.625 (µm) with power of $1.714 \cdot 10^{-9}$ (W). The sources are modelled as

plane wavefronts at the ELT entrance, which allows to represent the pupil shape with central obscuration and spiders.

In the following we consider the straylight analysis modes shown in Figure 2 one-by-one and interpret the results.

2. SCATTERED LIGHT IN DIRECT IMAGING MODES

2.1 Scattering model

The radiation scattering on optical surfaces is computed with the K-correlation model.[3] It allows to explicitly take into account the root mean square (RMS) roughness of the surface when computing the bidirectional scattering distribution function (BSDF) of the surface. Also, this model is already implemented in Zemax Optics Studio. The BSDF is defined as

$$BSDF(\beta, s \neq 2) = \frac{2\pi dn^2 RB^2}{\lambda^4} \frac{\sigma^2(\lambda)(s-2)}{\left[1 - [1 + B^2/\lambda^2]^{1-s/2}\right]} \frac{cos(\theta_i)cos(\theta_s)}{[1 + B^2\beta^2/\lambda^2]^{s/2}}, \tag{1}$$

$$BSDF(\beta, s = 2) = \frac{4\pi dn^2 RB^2}{\lambda^4} \frac{\sigma^2(\lambda)}{ln(1 + B^2/\lambda^2)} \frac{cos(\theta_i)cos(\theta_s)}{[1 + B^2\beta^2/\lambda^2]}. \tag{2}$$

Here λ is the measurement wavelength in microns, s – slope of BSDF function at large spatial frequencies, B – 2π times the typical surface wavelength L, $\sigma(\lambda)$ –total effective RMS roughness over frequencies from 0 to $1/\lambda$ in microns, R – surface specular reflectivity, dn – change in index of refraction at the surface (=2 for mirrors), θ_i – angle of incidence – relative to surface normal, θ_s – scatter angle – relative to surface normal, β – sine of the scatter angle minus sine of specular reflection angle $\beta - \beta_0$. The total integral scattering (TIS) is defined as:

$$TIS(\sigma, \lambda) = 4\pi^2 dn^2 \frac{\sigma^2(\lambda)}{\lambda^2}. \tag{3}$$

If the roughness was characterised for one wavelength λ_0 and applied at another wavelength λ, it should be recomputed by

$$s \neq 2; \frac{\sigma^2(\lambda)}{\sigma^2(\lambda_0)} = \frac{\left[1 + [1 + B^2/\lambda^2]^{1-s/2}\right]}{\left[1 + [1 + B^2/\lambda_0^2]^{1-s/2}\right]}, \tag{4}$$

$$s = 2; \frac{\sigma^2(\lambda)}{\sigma^2(\lambda_0)} = \frac{ln(1 + B^2/\lambda^2)}{ln(1 + B^2/\lambda_0^2)}. \tag{5}$$

The parameters of K-correlation model, namely the slope s and typical surface wavelength were calibrated by fitting the data known from literature. The system includes superpolished golden mirrors, $ZnSe$ and CaF_2 plates. For the mirrors the calibration data is taken from[4] . The model fitting for polished $ZnSe$ and CaF_2 surfaces is made in the same way using the data from[5] . The fitting results are shown in Figure 4.

The obtained model parameters are summarized in Table 1. Note that the B values for mirror and $ZnSe$ plate are extremely high. If B is defined as essentially equal or larger than the size of the part, then the K-Correlation model becomes fractal (constant log-log slope). So, with the obtained B values BSDF never reaches a roll-off point and one may assume that the exact value of B is not important, it is just larger than any clear aperture diameter and the calculated value was kept in all the simulations. Hereafter we assume that the model can be scaled only by changing the σ, while the B, s and dn parameters are maintained for the same material and polishing technique.

Further we apply these models for each type of optical element to model the scattering. We consider two scenarios:
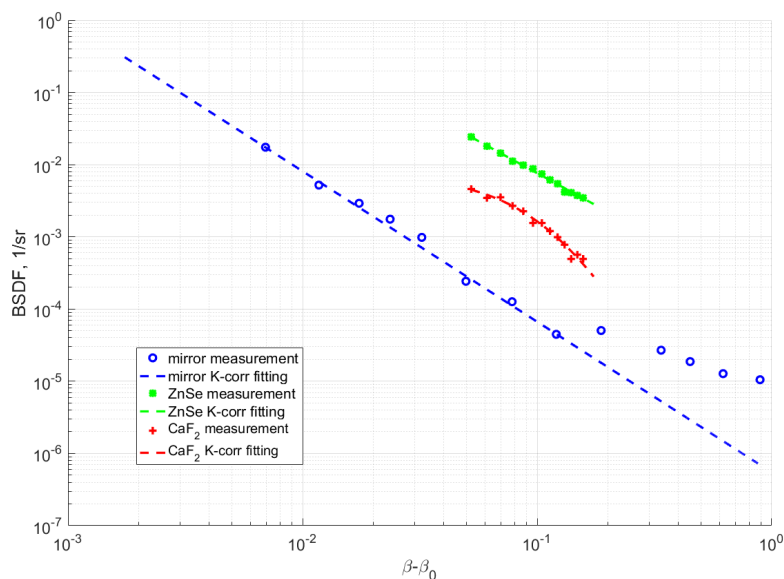
Figure 4. The BSDF data for different surface types calibrated with the K-correlation model.

Table 1. Parameters of the calibrated K-correlation models.

Material	σ_0 (nm)	dn	λ_0 (nm)	B (mm)	s
Mirror	1.9	2	3.39	28933	2.08
ZnSe	21.7	1.425	3.39	1213.7	1.779
CaF_2	17.6	0.421	3.39	27.3	6.04

A – Baseline with 1 (nm) RMS roughness for the CFO mirrors, cryostat window and the SCAO dichroic and 2 (nm) RMS for the rest of the components;

B – Worst case with 5 (nm) RMS roughness for all of the components.

Each time the corresponding TIS is computed according to (3) and substituted to the model.

2.2 Coatings

The K-correlation model picks up the reflection/transmission from the surface properties, so the actual coating properties must be defined in the optical system model. The coatings are defined as follows:

1. The anti-reflection (AR) coating on the cryostat window is defined according to the instrument specification with the average transmission over the waveband greater than 86% and minimum transmission including the substrate absorption greater than 80% at any point.

2. The AR coatings for the rest of the ZnSe elements are defined according to a real NSE-AI114 coating from Knight Optical.[6]

3. The AR coating on the CaF_2 elements has a constant residual reflecion of 2% according to the instrument specifications.

4. The dichroic coating on the beam-splitter coupling CFO and SCAO subsystems is defined according to the specifications and has the reflection varying from 68 to 78% in the range of 1.15 to 2.45 (μm) and transmission of 89.2 to 99.9% in the range of 2.7 to 10.7(μm).

5. Similarly, the properties of dichroic separating the imager's LM and N branches is defined according to the specifications with up to 97.8% transmission below 5.9 (μm) and $59.4 - 98.9\%$ reflection above it.

6. The imager detectors have AR coating defined according to the data provided by the manufacturers: the residual reflection of the LM band detector is $0.4 - 30.5\%$ and for the N band detector, it is $0.3 - 27.5\%$.

7. The science filters properties are set up according to the specifications and properties of the imaging filters offered for NaCo.[7] We use the L' filter with $92 - 95\%$ transmission in $3.55 - 4.07$ (μm) and N_2 filter with 85% transmission in $10.1 - 13.1$ (μm).

8. The neutral density (ND) filters in both branches of the imager are presented as partially reflective surfaces with a constant transmission of 10%.

2.3 Scattered light simulation

The scattered light is estimated for two monochromatic sources as described in Section 1. We consider only on-axis sources, in this case the scattered light cropping by the baffles and mechanical structure is minimal. The raytracing is performed with 10^6 rays and 10^7 attenuation threshold. The simple splitting algorithm is used to exclude ghosts from the simulated images to be processed. Note, that the simple splitting algorithm doesn't completely exclude the ghosts generation. But in this particular case for all the ghost-producing surfaces as the cryostat window, ADC-s and the dichroic beam-splitters, the transmission is substantially higher than the residual reflection, so the reflected rays are not generated. There are no evidences of the double-reflection ghosts in the simulated images presented below and this way to exclude them was found to be more efficient than post-processing of a simulated frame, which contains ghosts. In fact, elimination of the ghosts in the simulated image is necessary to separate the scattering and multiple-reflections mechanisms contributions, since they are defined by different requirements. The importance sampling algorithm is applied in order to increase the ray tracing efficiency. For each component the scattering targets represent spheres centered around the two adjacent components (one upstream the optical train and one downstream) with the radius larger than the component's full aperture radius by 5 (mm). The core of the image is detected by an absorbing square detector with 250x250 pixels covering $0.03 \times 0.03 (\text{arcsec}^2)$ on the sky. The scattered light is detected by a transmitting square detector with 250x250 pixels covering $2.7 \times 2.7 (\text{arcsec}^2)$ area on the sky. The pixel size in this case is 18 (μm), which corresponds to the real pixel size. The raytracing was performed in the described way for all configurations. Figure 5 shows the two simulated images for the LM branch with baseline surface roughness (the IMG platescale is 0.3 (arcsec/mm)).
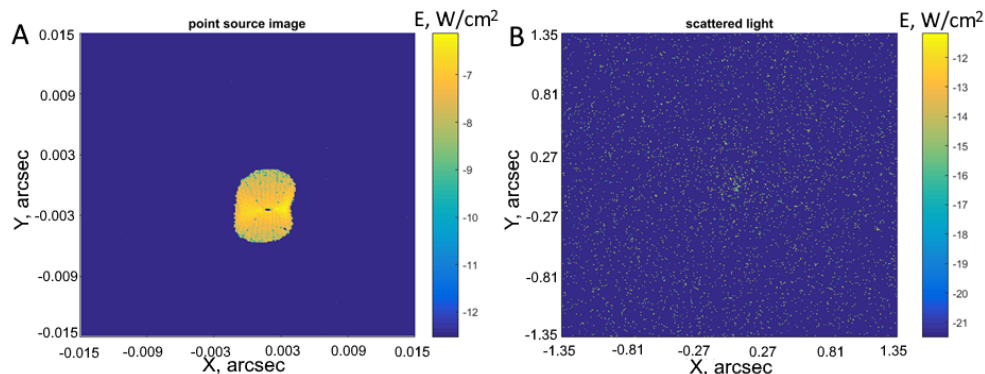

Figure 5. Raytracing results for the nominal roughness in LM band (logscale): A – image core, B – irradiation scattered in a wide angle.

The other 3 configurations were modeled in a similar way. The requirement to scattering from in-field sources in imaging mode is defined as a limit on the ratio between the maximum scattered flux to the entire flux coming into the image, i.e.

$$A = \frac{\Phi_{sc.max}}{\Phi_{im.tot}} = \frac{max(max(E_2))p_2^2}{\sum\sum E_1 p_1^2}, \tag{6}$$

where E_1 and E_2 are the output irradiation matrices of the small and large detectors, respectively, and p_1 and p_2 are the corresponding pixel sizes. The scattered light fraction in different modes computed according to (6) is shown in Figure 6.
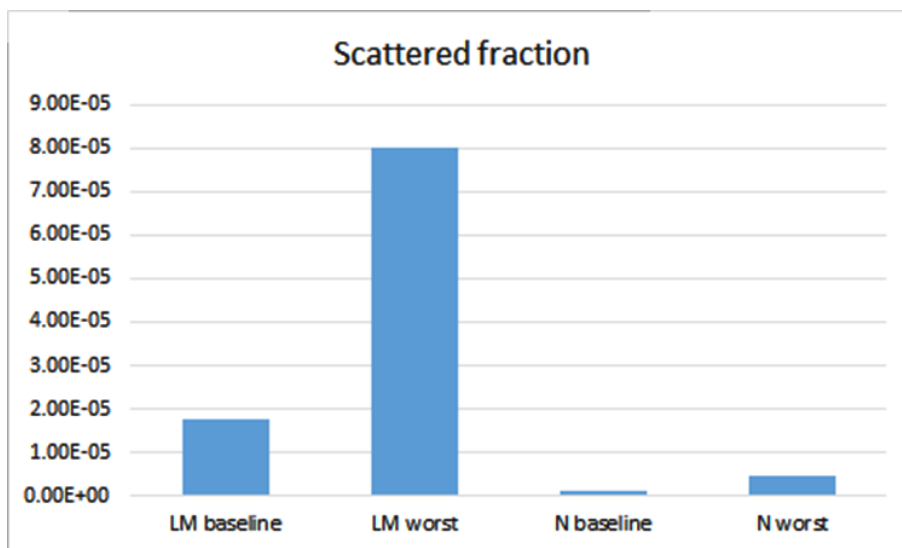

Figure 6. The scattered light attenuation levels found by raytracing in different modes.

The diagram shows that the maximum value is $7.99 \cdot 10^{05}$ for the LM band worst case. Comparing this value with the target scattered level of 10^{-3} defined by the science goals (IMG-1) we can conclude that the level of scattered light is more than 1 order of magnitude lower than the requirement even for the worst case, which provides a good safety margin.

3. GHOSTS IN DIRECT IMAGING MODES

The ghosts modelling is performed in two different modes with specific settings of the system model: A – Ghosts identification used to specify the surfaces creating the ghost and estimate the intensities. B – Datacube forming used for tracking the ghosts evolutions with moving and retracting of the optical components.

In both of the cases all the assumption regarding the probing sources wavelenghts and power, coatings and mechanical model representation remain valid.

3.1 Ghost identification

In this mode only on-axis sources are traced. Three detectors are used, namely: IMG core – 10×10 pixels with the angular size is $0.054 \times 0.054 (\text{arcsec}^2)$, IMG full – 2200×2200 pixels with the angular size is $11.8 \times 11.8 (\text{arcsec}^2)$ and IMG undersampled – 12×12 pixels with the angular size is $11.8 \times 11.8 (\text{arcsec}^2)$. Note that the full image is detected with two detectors to account for different sensitivity for a point and extended object. For the core and full detectors the pixel size is 18 (μm), which corresponds to the actual value. The full and undersampled detectors are 10% oversized to identify the ghosts in the proximity of the sensitive area.

The raytracing is performed for 5000 rays with the attenuation threshold of 10^7 in a loop. The full raysplitting algorithm was used and the scattering wasn't taken into account. At each step of the loop one real transmitting surface along the optical train was replaced by a perfectly transmitting one and the ghosts disappearing after such a substitution were assigned to this surface. Some surfaces can reflect the ghost-forming beam twice. The

number of reflections is derived from the relative ghost intensity. The results of ghost identification are shown in Figure 7. Note that the ghosts coming from all other possible combinations of reflections are below the set attenuation threshold. The identified contributing surfaces combinations are as follows:

A - ADC2 surf.2+SCAO dichroic surf.1+ SCAO dichroic surf.2+LM neutral filter surf.1

B - ADC1 surf.1+SCAO dichroic surf.1+ SCAO dichroic surf.2+LM neutral filter surf.1

C - ADC2 surf.1+SCAO dichroic surf.1+ SCAO dichroic surf.2+LM neutral filter surf.1

D - ADC1 surf.2+SCAO dichroic surf.1+ SCAO dichroic surf.2+LM neutral filter surf.1

E - ADC1 surf.1+ADC2 surf.1

F - ADC1 surf.1+ADC2 surf.1+LM neutral filter surf.1 + IMG LM detector

G - SCAO dichroic surf.1+ SCAO dichroic surf.2

H - Cryostat window WIN surf.1+Cryostat window surf.2

I - ADC1 surf.2+ADC2 surf.1

J - ADC1 surf.1+ADC2 surf.2

K - Cryostat window surf.1+SCAO dichroic surf.1+ SCAO dichroic surf.2 x2

L - Cryostat window surf.1 x2+Cryostat window surf.2 x2

M - Cryostat window surf.1 x2 + Cryostat window surf.2 x2;

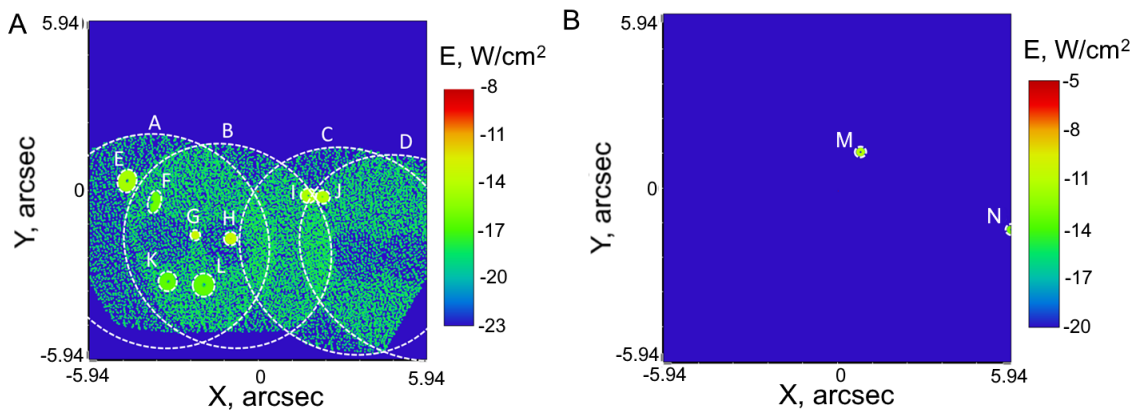N - Cryostat window surf.1 + Cryostat window surf.2.

Figure 7.   Ghosts in the direct imaging mode: A – LM band, B – N band.

Then we estimate the ghosts intensities in comparison with the detectors sensitivity and the background irradiation. The probing sources power can be converted to the flux density in (Jy) as

$$S = \Phi \frac{1}{c/\lambda_1 - c/\lambda_2} \frac{1}{\pi D^2/4} 10^{23}, \tag{7}$$

where Φ (W) is the source power, c (m/s) is the speed of light, $\lambda_1..\lambda_2$ (m) is the filter bandwidth, and D (m) is the ELT primary mirror diameter. Substituting the sources power values and the filter's bandwidths of

$3.49 - 4.01$ (µm) and $10.15 - 13.10$(µm) for the L' and N_2 wavelengths, respectively gives us the flux densities of $S_{L'} = 59.2$ (mJy) and $S_{N2} = 21.4$ (Jy). Using the normalized ghosts intensities as attenuation factors one can compute the corresponding ghost flux densities and compare them with the detectors sensitivity threshold. We presume the median conditions and consider the peak ghost irradiation everywhere. The computation results are shown in Table 2.

The irradiance values in the point source image are $E_{L'} = 7.617 \cdot 10^{-9}$(W/cm^2) and $E_{N2} = 2.812 \cdot 10^{-6}$(W/cm^2). Assuming linear transfer everywhere we can obtain the correspondence transfer coefficients of 957.38 and 1640.7 for the LM and N band, respectively. The sky background flux taken from SkyCalc[8] can be converted into a power of elliptical source covering ELT M1 as follows:

$$\Phi = \frac{\Delta\lambda^2 \sum B_{SkyCalc}/\lambda hc (2y')^2 D^2/4}{(\lambda_2 - \lambda_1)PS}, \tag{8}$$

where $h, (\mathrm{J} \cdot \mathrm{s})$ is the Planck constant, $\Delta\lambda$ (µm) is the SkyCalc wavelength scanning period, $PS = 0.3316$(cm/arcsec) is the platescale, $2y' = 3.67$(cm) is the image area at ELT focus. These computations return the background equivalent source power equal to $2.351 \cdot 10^{-7}$(W) and $1.502 \cdot 10^{-5}W$ for L' and N_2, respectively. Applying the estimated transfer coefficients and the computed attenuation factors we can also assess the ghost as a fraction of background flux (Table 2).

Table 2. Ghost intensities in the direct imaging mode.

Probing wavelenght	L'	N_2
Point source mode ghost flux density (Jy)	$8.166 \cdot 10^{-7}$	$8.671 \cdot 10^{-5}$
Extended source mode ghost flux density (Jy/arcsec^2)	$1.848 \cdot 10^{-8}$	$1.725 \cdot 10^{-6}$
Point source mode sensitivity, (Jy)	$0.587 \cdot 10^{-6}$	$1.285 \cdot 10^{-4}$
Extended source mode sensitivity (Jy/arcsec^2)	$1.230 \cdot 10^{-3}$	$2.915 \cdot 10^{-2}$
Background equivalent irradiation (W/cm^2)	$2.251 \cdot 10^{-4}$	$2.460 \cdot 10^{-2}$
Peak ghost irradiance (W/cm^2)	$1.051 \cdot 10^{-13}$	$1.142 \cdot 10^{-11}$
Ghost as the background fraction	$4.670 \cdot 10^{-10}$	$4.642 \cdot 10^{-10}$

The found attenuation factors values lead to ghosts, which are at least one order of magnitude fainter than the detectors sensitivities thresholds. When compared to the background equivalent flux under a few presuptions, the ghosts appear to be $4.6 \cdot 10^{-10}$ fainter. This shows a good safety margin for the ghost suppression in this operational mode (IMG-2).

3.2 Ghost datacube

In order to track the movement and intensity changes of the ghosts and simulate the image processing a datacube was formed. Each layer of the datacube represents a simulated image similar to that shown in Figure 7 for different system configurations.

The 3 probing sources at 0, 1" and 5" in +Y direction to form the datacube, while the wavelenghts and power values are the same.

The output is read out from 3 detectors with the following parameters: CFO FP2 – 501×501 pixels, the angular size is 27.64×27.64(arcsec^2); IMG N – 501×501 pixels, the angular size is 11.8×11.8(arcsec^2); IMG LM – 501×501 pixels, the angular size is 9.8×9.8(arcsec^2).

The following components properties and positions are considered as variables causing the ghost movement and forming the datacube in a nested loop:

1. Derotator in 3 positions : $0, 90$ and $180°$ field rotation;

2. Pupil stabilization mirror in 3 positions: $0, +0.041°$ in X direction and $+0.041°$ in Y direction – corresponding to 5% of the pupil;

3. Chopper in 3 positions: $0, +0.426°$ in $+X$ direction and $+0.426°$ in $+X$ direction , corresponding to $+5arcsec$ on sky;

4. 2 perfectly absorbing field masks at FP2 with clocking rotation matching the field clocking: FIELD-11 , square with 32.1 (mm) side and FIELD-14, square with 44.68 (mm) side;

5. LMS pick-off splitter in 2 positions – on/off. LMS has a mount with elliptical opening 20x28 (mm).

The raytracing is performed with 200 rays per configuration and 10^7 attenuation threshold in ZemaxOptics Sudio under control of a Matlab script through ZOS-API. The output is in 3 files for FP2 in direct propagation, LM IMG and N IMG focal planes. The files are 251001*108 elements arrays in *.fits* format. Each column is one configuration and each row is a 501*501 pixels image reformatted to a vector. This datacube will be used to simulate the data reduction and calibration in the METIS images and estimation of the residual ghosts intensity as a fraction of the background according to the top=-level requirements.

4. STRAYLIGHT IN HCI MODES

METIS has 6 pure HCI modes and 8 modes of HCI in combination with spectroscopy.[9] The analyses are performed for 2 HCI modes, namely

1. Ring apodizer vortex coronagraphy (RAVC) in LM with ring apodizer plate (RAP) in CFO pupil plane, vortex phase mask (VPM) in CFO focal plane and Lyot stop coronagraph in IMG pupil plane.

2. Apodizing phase plate coronagraphy (APP) in LM with apodizing phase plate (APP) in IMG pupil plane.

The other modes are supposed to be similar or less risky in terms of straylight due to the smaller number of components and/or longer wavelenghts. It should be noted here that all the straylight artifacts in HCI modes falling within the dark hole with $0.85arcsec$ readius around the image center must be below 10^{-5} in relative intensity. So all the requirements HCI-1 to HCI-5 are appplied similary.

4.1 HCI ghosts

The RAVC-LM mode uses 3 specific components:

1. The RAP represents a 6 (mm) thick ZnSe substrate with the front surface split into 3 zones having the throughput of 75, 100 and 0%, respectively.

2. The VPM is a combination of

   - A $0.2 \times 0.2(mm^2)$ perfectly absorbing rectandular detector in the center of CFO focal plane used to measure the flux power reaching VPM and assign the power of secondary source,

   - The VPM substrate representing 0.3 (mm) thick CVD diamond plate with a 95%-efficient antireflective , which approximately represents the total transmission of an annular groove grating etched onto the first surface ($\approx 95\%$) and a 2D square grating etched on its second surface ($\geq 99\%$),

   - Secondary source modelling the radiation deflected by VPM in a wide angle. It uses the algorithm and software tools developed by Andre Bone.[10] The secondary source has power of $2.013 \cdot 10^{-12}$(W), source radius 0.0257(mm) (corresponds to $0.5\lambda/D$), $F/\# = 17.452$ and the aperture parameters following the ELT M1. The secondary source model creates a peculiar irradiation pattern 100 mm away from the focal plane (Figure 8, A). Then the most of the rays coming from the on-axis source are blocked by the Lyot stop (Figure 8, B). However, due to double reflections some portion of light may pass through the stop and create a ghost (Figure 8, C).
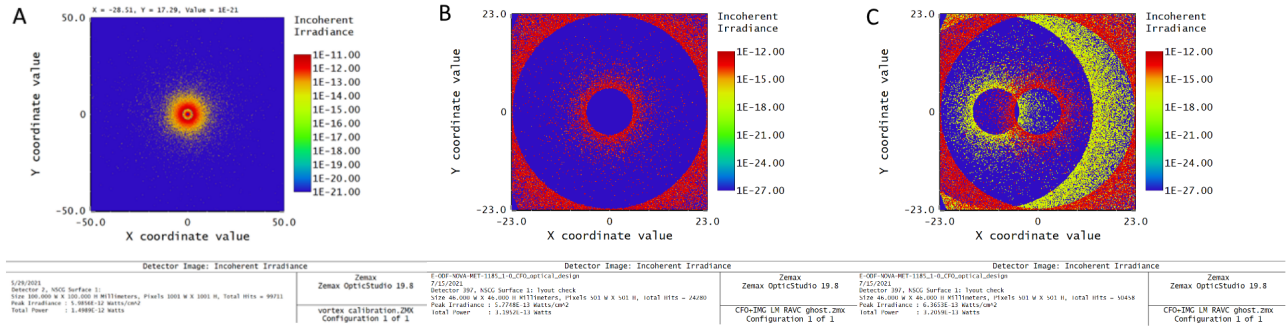
Figure 8. Emission pattern of the secondary source representing VPM: A — 100mm from the focal plane, B –– IMG pupil plane, C — IMG pupil plane with double reflections.

3. The RLS represents an amplitude mask drilled into a metal plate, which follows the ELT pupil with an undersizing.

The results obtained with 20 000 rays traced and 10^7 attenueation thershold are shown in Figure 9, A. After the raytracing all the irradiation values were normalized to that in the non-coronographic PSF, which is understood as the nominal imaging PSF corrected for the HCI components throughput and not taking into account the VPM deflection properties. The rays, which are deviated by the VPM and not blocked by the Lyot stop, create a concentrated ghost with the relative intensity of $1.6 \cdot 10^{-3}$. However, it is perfectly centerd and cannot affect the scientific image. For this reason this ghost was artificially removed from the simulated frame. The rest of the ghosts seen in the image don't exceed the relative intensity of $2.69 \cdot 10^{-7}$ and placed outside of the 0.85(arcsec) - dark hole, which is the critical zone for HCI observations.

The APP-LM mode uses only one specific component, namely the apodizing mask. It represents a reflective surface, which geometry follows the pupil image at IMG PP with 4% undersizing. The mask is imposed on a 6mm-thick *ZnSe* substrate with 0.3° wedge and AR coating identical to that used in Sect. 2.2. The raytracing results obtained with the same settings are shown in Figure 9, B. The ghosts were identified similarly to Sect. 4.3. The focused ghosts are moved away from the critical zone by introducing the substrate wedge. Only defocused ghosts coming from the APP mask are present within the dark hole and their maximum relative intensity is $6.57 \cdot 10^{-6}$.
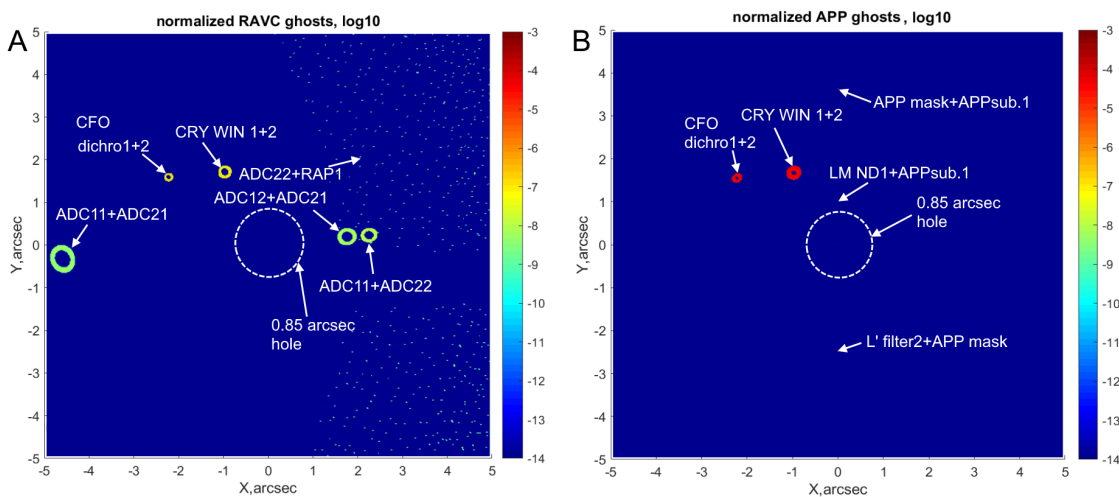

Figure 9. Ghost identification in HCI modes: A — RAVC-LM mode, B –– APP-LM mode.

4.2 HCI scattering

The surface roughness of all the optical components is identical to the baseline roughness level considered in Sect. 2.3. The specific HCI components roughness values are set as follows: 2 (nm) as the baseline and 5 (nm) as the worst case for the RAP and APP mask; 15 (nm) as the baseline and 20 (nm) as the worst case for the VPM. The TIS was computed by (3). The raytracing was performed with 10^6 rays and 10^7 attenuation threshold with the settings identical to those used before. The central ghost appearing in the RAVC mode due to the VPM leakage was artificially cropped from the simulated frame to analyse the scattering contribution separately from the ghosts. The scattering intensities normalized to that of non-HCI PSF are shown in Figure 10. The diagram shows that the scattering level remains safe for the baseline roughness, though in the worst cases it may exceed the target level of 10^{-5}.
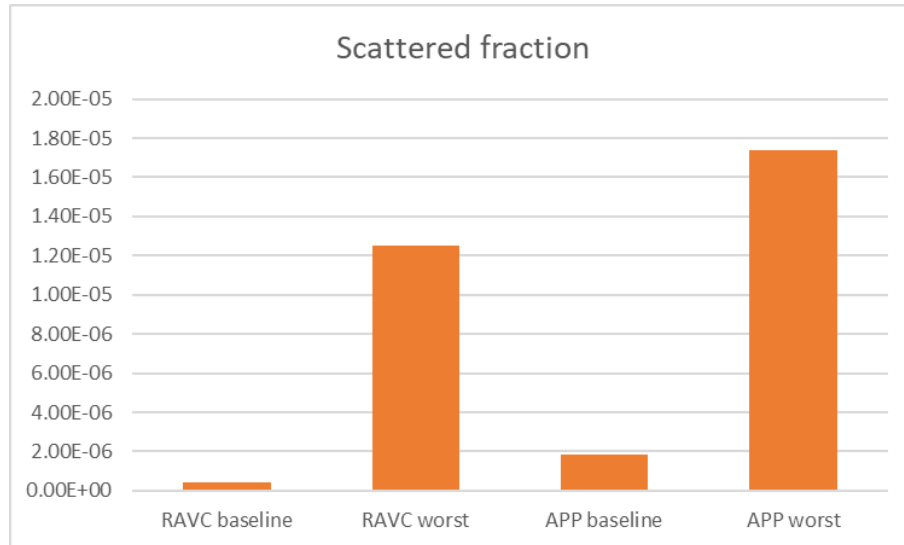

Figure 10. The scattered light attenuation levels found by raytracing in HCI modes.

4.3 Dust and defects influence in HCI

Contamination and surface defects such as scratches and digs will contribute to the scattered light and decrease the image contrast in a several ways. They can cause diffraction scattering, pupil plane shadowing and shadowing or direct obscuration in the proximity of the focal planes. In contrast with the other straylight mechanisms the influence of dust and surface defects was estimated analytically, since it is difficult to model it directly. The direct imaging modes appear to be quite insensitive to these effects, so the analysis is driven by the HCI requirements completely. Meanwhile, this simplified analytical approach doesn't account for any specific HCI effects as the VPM diffraction or APP efficiency. We assume that only the surfaces close to the cardinal planes as focal and pupil planes are taken into account and that contributions from different surfaces and different mechanism are summed quadratically and the target straylight level of 10^{-5} was divided subsequently. As the results for the baseline scenario in Figure 10 show that the roughness contribution almost 1 order of magnitude below the limit, it is not taken into account in this analysis. The entire analysis algorithm follows that used for the SPHERE instrument.[11]

The cleanliness requirements were converted to the relative units defined my the MIL standard.[12] The obtained values are summarized in Table 3

Similarly, the requirements for the critical surfaces defects were computed for the case of equal contribution of digs/short scratches and long scratches. The obtained values were converted to the requirements according to standard[13] and summarized in Table 4.

Table 3. Component cleanliness requirements.

Component	Mechanism	Particle size (μm)	Particle density (1/0.1m^2)	Cleanliness level
ADC's	Pupil shadowing	12	2450	264
Derot. mirror 3	Image shadowing	169	990	1095
Pupil stab. mirror	Image shadowing	140	1370	1017
Chopper mirror	Pupil shadowing	37	3270	501
LMS pick-off	Image shadowing	25	19090	578
VPM	Image obscuration	52.4	10	102
APP	Pupil shadowing	28	5910	481
Detector	Image obscuration	1.5	57	33

Table 4. Surfaces scratch and dig requirements.

Component	Square root of short scratches area (mm)	Long scratch width (mm)	ISO standard requirement
Derot. mirror 3	0.61	0.011	5/ 5x0.63 L1x0.01
Pupil stab. mirror	0.51	0.009	5/ 5x0.4 L1x0.01
LMS pick-off	0.30	0.017	5/ 5x0.25 1x0.016

5. STRAYLIGHT MITIGATION

The measures to mitigate the straylight are considered throughout the design process. They include:

1. Parameters of the nominal optical system design as collimators oversizing to account for the HCI elements scattering, using filters to avoid out-of-band straylight, pupil stops to limit prevent the telescope thermal emission from reaching the detectors, design parameters of the ADC and tilt/wedge angles of the transmission components and detectors to defocus and move the ghost images.

2. Specific points in the optical components and assemblies specification derived from the analyses described above. They include the low surface roughness values and scratch and dig requirements to be specified in the optics drawings, as well as the allowable levels of cleanliness and indication of the critical components, which require special protection of dust during the assembling and integration.

3. Optomechanical design, which implies using baffles and black coatings along the entire optical train. This measure is critical to supress the out-of-beam straylight (IMG-5 and HCI-5) but will also affect other straylight origins. The baffles should represent a structure with orthogonal vanes (Figure 11,A), which guarantee that any out-of-beam ray will be reflected at least twice before leaving the baffle.[14] Although, baffles with co-axial vanes or light traps can be used for some critical components, or those, which cannot be approached closely (Figure 11,B). All of these elements should be coated by a specific black coating as Acktar Fractal ^{TM}[15] or similar.

6. CONCLUSIONS

In the current paper we investigated straylight in the ELT-METIS instrument originated from different sources for the most critical instrument configurations. The approach relies on detailed bottom-up modelling and it has demonstrated that with the current optical design and baseline requirements of the optical components the expected straylight level should be compliant with the requirements derived from the science goals both in direct imaging and high-contrast imaging modes.
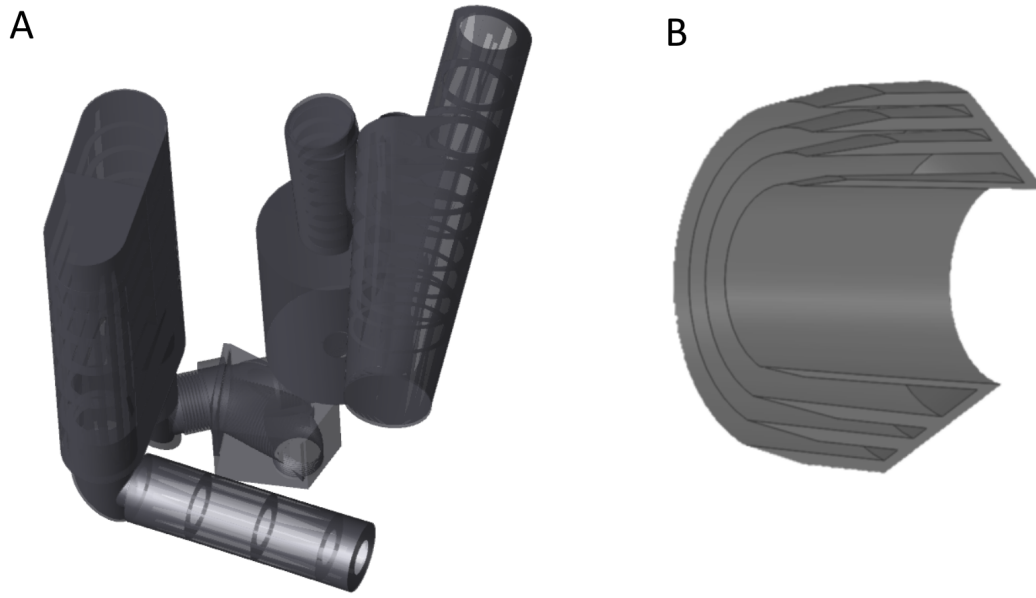
Figure 11. Exemplary METIS baffles design: A – general view of baffles with orthogonal vanes for CFO, B – light trap with co-axial vanes for LMS pick-off splitter.

The results obtained at this stage will be used for the specifications of the METIS optics, the design of opto-mechanical components and additionally the definition of the subsequent alignment, integration and tests phase.

Since the METIS performance goals are high and sensitive to second-order factors as the straylight, the analyses are more detailed than those carried out for other instruments like VLT-VISIR.[16] So the present study may be useful for design and analysis of the future high-precision instruments.

REFERENCES

[1] Brandl, B. R., Absil, O., and Agocs, T., "Status of the mid-IR ELT imager and spectrograph (METIS)," in [*Ground-based and Airborne Instrumentation for Astronomy VII*], Evans, C. J., Simard, L., and Takami, H., eds., **10702**, 582 – 596, International Society for Optics and Photonics, SPIE (2018).

[2] Brandl, B., Bettonvil, F., van Boekel, R., Glauser, A., Quanz, S., Absil, O., Amorim, A., Feldt, M., Glasse, A., Güdel, M., Ho, P., Labadie, L., Meyer, M., Pantin, E., van Winckel, H., and METIS Consortium, "METIS: The Mid-infrared ELT Imager and Spectrograph," *The Messenger* **182**, 22–26 (Mar. 2021).

[3] Dittman, M. G., "K-correlation power spectral density and surface scatter model," in [*Optical Systems Degradation, Contamination, and Stray Light: Effects, Measurements, and Control II*], *Proc. SPIE* **6291**, 62910R (2006).

[4] Wang, Y. and Wolfe, W. L., "Scattering from microrough surfaces: comparison of theory and experiment," *J. Opt. Soc. Am.* **73**, 1596–1602 (1983).

[5] Sorensen, K., Lee, W. W., and Scherr, L. M., "Bidirectional transmittance distribution function of several infrared materials at 3.39 microns," in [*Scatter from Optical Components*], *Proc. SPIE* **1165**, 237–245 (1990).

[6] "Infrared Coatings." Knight Optical Official website, 28 October 2013 https://www.knightoptical.com/infrared-coatings/. (Accessed: 14 July 2021).

[7] "List of imaging filters offered for NaCo." ESO Official website, 29 September 2019 http://www.eso.org/sci/facilities/paranal/decommissioned/naco/inst/filters.html. (Accessed: 14 July 2021).

[8] "SkyCalc Web Application Version 2.0.9." ESO Official website, 9 May 2020 https://www.eso.org/observing/etc/doc/skycalc/helpskycalc.html. (Accessed: 14 July 2021).

 [9] Carlomagno, B., Delacroix, C., and Absil, O., "METIS high-contrast imaging: design and expected performance," *Journal of Astronomical Telescopes, Instruments, and Systems* **6**(3), 1 – 30 (2020).

[10] Bone, A., [*Mechanical and Optical Studies for an Extremely Large Telescope Mid-Infrared Instrument, PhD Thesis*], Lisbon Univ, Lisbon (2020).

[11] Beuzit, J.-L., "Sphere: the exoplanet imager for the very large telescope," *A&A* **631**, A155 (2019).

[12] "MIL-STD-1246C, Product Cleanliness Levels and Contamination Control Program." (14 July 2021).

[13] "ISO 10110, Optics and photonics — Preparation of drawings for optical elements and systems — Part 7: Surface imperfections, Ed.3." (Aug 2017).

[14] Fest, E., [*Stray Light Analysis and Control*], SPIE, Bellingham (2013).

[15] Montemurro, L., Zanetti, F., and Simone, A., "Black coatings for combined stray light and thermal passive management for the challenging environmental conditions of Solar Orbiter," in [*International Conference on Space Optics — ICSO 2018*], Sodnik, Z., Karafolas, N., and Cugny, B., eds., **11180**, 1853 – 1859, International Society for Optics and Photonics, SPIE (2019).

[16] Rio, Y., Lagage, P.-O., Dubreuil, D., Durand, G. A., Lyraud, C., Pel, J.-W., de Haas, J. C., Schoenmaker, A., and Tolsma, H., "VISIR: the mid-infrared imager and spectrometer for the VLT," in [*Infrared Astronomical Instrumentation*], Fowler, A. M., ed., **3354**, 615 – 626, International Society for Optics and Photonics, SPIE (1998).